

The Gel'fand-Levitan-Krein method and the globally convergent method for experimental data

Andrey L. Karchevsky[•], Michael V. Klibanov^{*}, Lam Nguyen[△],
Natee Pantong^{**} and Anders Sullivan[△]

[•] Sobolev Mathematical Institute, 4 Acad. Koptyug Ave, Novosibirsk, 630090, Russia,
karchevs@math.nsc.ru

^{*} Department of Mathematics and Statistics, University of North Carolina at Charlotte,
Charlotte, NC 28223, USA, mklibanv@uncc.edu

[△]US Army Research Laboratory, 2800 Powder Mill Road Adelphi, MD 20783-1197, USA,
lam.h.nguyen2.civ@mail.mil and anders.j.sullivan.civ@mail.mil

^{**} Department of Mathematics and Computer Science, Royal Thai Air Force Academy, Bangkok,
Thailand, npantong@hotmail.com

Abstract: Comparison of numerical performances of two methods for coefficient inverse problems is described. The first one is the classical Gel'fand-Levitan-Krein equation method, and the second one is the recently developed approximately globally convergent numerical method. This comparison is performed for both computationally simulated and experimental data.

2010 AMS subject classification: 35R25, 35R30

Keywords: 1-d Coefficient Inverse Problems, comparison of two methods, calibration factor

1 Introduction

The goal of this publication is to compare performances of two numerical methods listed in the title on both computationally simulated and experimental data. The reason why we do not compare other methods is a practical one: such a study would require much more time and effort than the authors can afford to spend. We work with the time resolved data of scattering of the electrical wave field and these data are the same as ones in [24]. The data were collected in the field in the cluttered environment by the Forward Looking Radar of US Army Research Laboratory (ARL) [30]. The goal of this radar is to detect and possibly identify shallow explosives.

1.1 Previous publications

In publication [24] the data of the current paper were successfully treated in the most challenging case: the case of blind data. To do this, the newly developed the so-called approximately globally convergent numerical method (AGCM) was applied. Since these experi-

mental data are the one-dimensional ones, then it is possible to use them for a comparison of numerical performances of the classical Gelfand-Levitan-Krein integral equation method (GLK) and AGCM. “Blind” means that first the data were delivered to the mathematical group by engineers of ARL, Sullivan and Nguyen, who coauthor both this paper and [24]. No information about targets was given to mathematicians, except their placements either above or below the ground. Next, the mathematical group made computations by AGCM and delivered results to engineers. Finally, engineers compared computational results with the truth and informed mathematicians about their findings, see Table 1 and Conclusion in subsection 3.5. The most important observation was that in all available sets of experimental data the values of computed dielectric constants of targets were well within limits tabulated in [32, 33]. Since dielectric constants were not measured in experiments, then this answer was a quite satisfactory one.

GLK was derived in 1950-ies by Gelfand, Levitan and Krein [16, 27, 22]. Originally it was derived for the 1-d inverse spectral problem. Later, it was shown in [12] that an inverse problem for the 1-d hyperbolic equation can be reduced to the GLK. In addition to [12], we also use here the material of §4 of Chapter 1 of the book [31], where the derivation of [12] is reproduced. As to the numerical results for GLK, we refer to interesting publications [1, 2, 3, 17, 28, 18, 19].

AGCM was developed for Coefficient Inverse Problems (CIPs) for the hyperbolic equation $c(x)u_{tt} = \Delta u, x \in \mathbb{R}^n, n = 1, 2, 3$ with single measurement data, see, e.g. papers [7, 8, 9, 20, 24, 25, 23] about this method; a summary of results is given in the book [6]. “Single measurement” means that the data are generated either by a single point source or by a single direction of the incident plane wave. Thus, single measurement means the *minimal amount* of available information. In particular, the performance of AGCM was verified on 3-d experimental data in [8, 6, 20]. All known numerical methods for n -d, $n > 1$ CIPs with single measurement data require a priori knowledge of a point in a small neighborhood of the exact coefficient. Unlike this, the *key advantage* of AGCM is that it delivers good approximations for exact solutions of CIPs without any advanced knowledge about small neighborhoods of those solutions. It is well known that this goal is an enormously challenging one.

Hence, a rigorous definition of the “approximate global convergence” property was introduced in [6, 9, 24, 25]. In simple terms, it means that first an approximate mathematical model is introduced. The approximation of AGCM is a mild one: it amounts to the truncation of an asymptotic series with respect to $1/s, s \rightarrow \infty$, where $s > 0$ is the parameter of the Laplace transform with respect to t of the above hyperbolic PDE. This truncation is done only on the first iteration. Next, a numerical method is developed within the framework of the resulting mathematical model. Next, a theorem is proved, which claims that this method delivers a good approximation for the exact solution of that CIP without any a priori knowledge of a small neighborhood of that solution. The common perception of global convergence is that one should obtain correct solution if iterations would start from almost any point. That theorem claims, however, that a small neighborhood of the exact solution is achieved if iterations would start not from any point but rather from a function which can be obtained without any knowledge of that small neighborhood. That theorem was

confirmed in numerical studies of both computationally simulated and experimental data. 3-d experimental data were treated in [8, 6, 20]. In particular, the most difficult blind data case was considered in [6, 20, 24]. We refer to the paper [29] and references cited there for another non-local method for a coefficient inverse problem.

1.2 A huge misfit between real and computationally simulated data

It was pointed out in all publications about AGCM for experimental data [8, 6, 20, 24] that there is a huge misfit between measured data and computationally simulated data, in the case of waves propagation in a non-attenuating medium. This misfit is evident from a simple visual comparison of simulated and experimental curves, see, e.g. Figures 3 and 4. This discrepancy is the main difficulty for the numerical treatment of experimental data by any computational method. In other words, the experimental data are lying far away from the range of the operator, which needs to be inverted to solve the CIP. It is well known that this is a compact operator. Hence, its range is very narrow and the inversion problem is unstable. Therefore, regularization is necessary. Still, the regularization theory gives recipes only in the case when the right hand side of the operator equation is not far from the range of that operator. However, in the case of those experimental data, the right hand side is actually far away from that range.

Therefore, the crucial step of all above cited publications about experimental data, was the data pre-processing procedure. This procedure has extracted such a piece of the data from the whole data, which looked somewhat similar with the computationally simulated data. Still, it was impossible to estimate the distance between the extracted data and the range of that compact operator. Furthermore, those data pre-processing procedures cannot be rigorously justified neither from the Physics nor from the Mathematics standpoint. They were based on the intuition only. The single criterion of their success was the accuracy of resulting solutions of corresponding CIPs. Since accurate results were obtained for the blind real data in [6, 20, 24], then those data pre-processing procedures were unbiased. We describe below the data pre-processing procedure. It consists of two steps: extracting a piece of data from the whole data and multiplying this piece by a calibration factor. This factor is unknown and needs to be determined numerically.

In section 2 we describe the experimental data we work with as well as the data pre-processing procedure. In section 3 we briefly describe the 1-d version of AGCM. GLK is described in section 4. In section 5 we compare performances of these two methods on our experimental data. We discuss results in section 6.

2 Experimental Data

2.1 Data collection

The time resolved nanosecond electric pulses are emitted by two sources installed on the radar (see Fig. 1). The schematic diagram of the data collection by the Forward Looking Radar is depicted on Fig. 2. Only one component of the electric field is both originated and measured in the backscattering regime. The data are collected by sixteen (16) detectors with the time step of 0.133 nanosecond. Only shallow targets placed either above or a few centimeters below the ground can be detected by this radar. This is sufficient for antipersonnel plastic land mines as well as for home made explosives. The depth of the upper part of the surface of a shallow underground target is a few centimeters. The Ground Positioning System (GPS) provides the distance between the radar and a point on the ground located above that target. The error in the latter is a few centimeters. Time resolved voltages of backreflected signals are integrated over radar/target distances between 20 meters and 8 meters, and they are also averaged with respect to both source positions as well as with respect to readings of sixteen detectors.

Since the radar/target distance is provided by GPS with a good accuracy, geometrical parameters of targets, including their depths, are not of an interest here. The main goal of the publication [24] was to calculate ratios R of dielectric constants

$$R = \frac{\varepsilon_r(target)}{\varepsilon_r(bckgr)}, \quad (1)$$

where $\varepsilon_r(target)$ is the dielectric constant of the background medium. If $\varepsilon_r(bckgr)$ is known, then (1) enables one to calculate $\varepsilon_r(target)$. If a target is located above the ground, then $\varepsilon_r(bckgr) = \varepsilon_r(air) = 1$. Unfortunately, dielectric constants were not measured during the data collection process. Therefore, the authors of [24] had no choice but to rely on tables of dielectric constants [32, 33] when evaluating the accuracy of results. In our mathematical

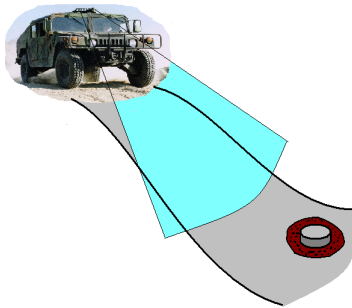


Figure 1: Schematic geometry of the forward looking radar

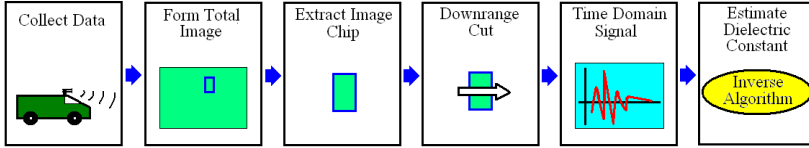


Figure 2: The schematic diagram of the data collection by the Forward Looking Radar

model (4)-(8) of section 3 R is the function of the spatial variable x , i.e. $R = R(x) := \varepsilon_r(x)$, $x \in (0, 1)$. Hence, after computing $R(x)$ we took the value \bar{R} to compute the dielectric constant of the target $\varepsilon_r(target)$, where

$$\bar{R} = \begin{cases} \max_{[0,1]} R(x) & \text{if } R(x) \geq 1, \quad \forall x \in (0, 1), \\ \min_{[0,1]} R(x) & \text{if } R(x) < 1, \quad \forall x \in (0, 1). \end{cases} \quad (2)$$

Hence, in (1) we actually have $R := \bar{R}$, and by (2)

$$\varepsilon_r(target) = \bar{R}\varepsilon_r(bckgr). \quad (3)$$

The importance of estimating dielectric constants of potential explosives is described in the following citation from the paper [24] “The recovered dielectric constant by itself is not a sufficient information to distinguish one target from another. The purpose of estimating the dielectric constant is to provide one extra piece of information about the target. Indeed, up to this point, most of the radar community relies solely on the intensity of the radar image for doing detection and discrimination of targets. It is hoped therefore that when the intensity information is coupled with the new dielectric information, algorithms could then be designed that will ultimately provide better performance in terms of probability of detection and false alarm rate”.

2.2 Severely under-determined data

The experimental data of both [24] and this paper are severely under-determined. We now describe main factors of the under-determination.

Since targets can be mixtures of constituent materials and since we had worked with 1-d data, whereas targets are certainly 3-d, then the calculated $\varepsilon_r(target)$ was a certain weighted average of the spatially distributed dielectric constant of a target. Due to some technical limitations, we possess only five sets of experimental data for five different targets. These targets are schematically depicted on the left panel of Fig. 3. For any target of interest, only a single time dependent curve can be extracted from the vast amount of data. The right panel of Fig. 3 depicts corresponding experimental curves, where the horizontal axis is time in nanoseconds. An important additional factor of the under-determination is the clutter surrounding targets. Other factors contributing to the under-determination were: the integration of all data as above, the unclear source position in (7), and it was also unclear where the time moment $t = 0$ is on the data.

2.3 Data pre-processing

We now describe the data pre-processing procedure. It consists of two stages.

2.3.1 First stage: selection of a single peak

Consider the mathematical model of the above process. Since only one component of the electric field was both sent into the medium and measured, and since we have received only one experimentally measured curve per target, we had no choice but to ignore the complete Maxwell's system and model the process by only one 1-d wave-like PDE. At the same time, recent computational testing of the full time dependent Maxwell's system in [11] has demonstrated that the component of the electric field $E = (E_1, E_2, E_3)$, which was originally sent into the medium, substantially dominates two other components. In addition, we refer to the accurate performance of AGCM for experimental data in [8, 6, 20], where only a single PDE, which was a 3-d analog of (6), was used for the mathematical model.

Let $u(x, t)$, $x \in \mathbb{R}$, $t > 0$ be the component of the electric field which is incident on the medium and which is also measured in the backscattering regime. Let $\varepsilon_r(x)$ be the spatially distributed dielectric constant of the medium. We assume that

$$\varepsilon_r(x) \in [d_0, d_1], \quad \varepsilon_r \in C^1(\mathbb{R}), \quad (4)$$

$$\varepsilon_r(x) = 1, \quad x \notin (0, 1), \quad (5)$$

where the numbers $d_0, d_1 > 0$. Thus, the interval $(0, 1)$ is our domain of interest in the CIP. We consider this interval as the one whose length is one meter. We model the process of waves propagation via the following hyperbolic Cauchy problem

$$\varepsilon_r(x)u_{tt} = u_{xx}, \quad x \in \mathbb{R}, \quad t \in (0, \infty), \quad (6)$$

$$u(x, 0) = 0, \quad u_t(x, 0) = \delta(x - x_0), \quad (7)$$

$$x_0 = -1. \quad (8)$$

Since the source position x_0 is unclear in our experiment (subsection 2.2), we choose $x_0 = -1$ in (8) for the sake of definiteness only.

Coefficient Inverse Problem 1 (CIP1). *Determine the coefficient $\varepsilon_r(x)$, assuming that the following function $g(t)$ is known*

$$u(0, t) = g(t), \quad t \in (0, \infty). \quad (9)$$

The function $g(t)$ models the backscattering data measured by the Forward Looking Radar. We now solve the forward problem (6)-(8) for the case when the graph of the function $\varepsilon_r(x)$ is the one depicted on Fig. 4-a). The resulting function $g_1(t) := g(t) - H(t - |x_0|)/2$ is depicted on Fig. 4-b). Here $H(t)$ is the Heaviside function and $H(t - |x - x_0|)/2$ is the solution of the problem (6)-(8) for the case $\varepsilon_r(x) \equiv 1$.

Comparison of Fig. 4-b) with the data depicted on the right panel of Fig. 3 confirms the above statement about a huge discrepancy between experimental and computationally

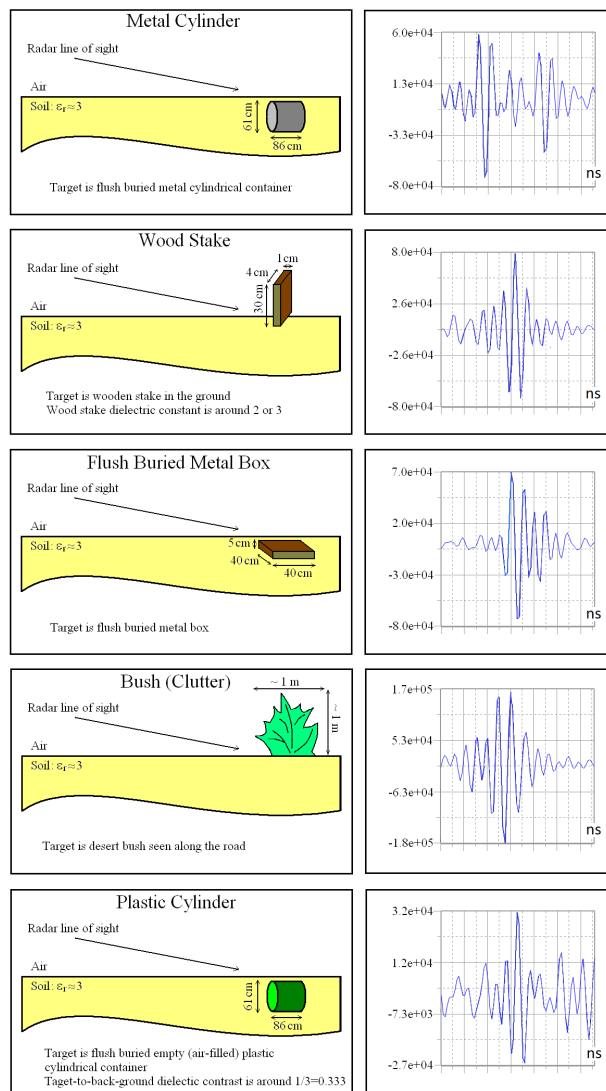


Figure 3: Targets and collected data before pre-processing

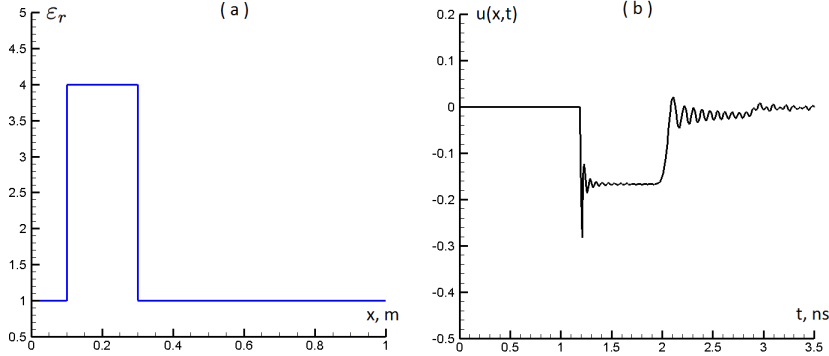


Figure 4: a) The graph of the function $\varepsilon_r(x)$ for which the data are computationally simulated via solution of the forward problem (6)-(8). b) The computed function $g_1(t) := g(t) - H(t - |x - x_0|)/2$ at the edge $\{x = 0\}$, where the backscattering data are collected. The function $g(t)$ is defined in (9)

simulated data. Therefore, we must change somehow the experimental data, i.e. pre-process it. So that the pre-processes data would look somewhat similar with the curve of Fig. 4-b). Observe that this curve has basically only one downward looking dent. If the step function of Fig. 4-a) would be downward looking, then we would have an upward looking step-like function on the corresponding analog of Fig. 4-b). Now, if a target is standing in the air, then the background medium is air with $\varepsilon_r(\text{air}) = 1$ and $\varepsilon_r(\text{target}) > 1$. Hence, it was decided in [24] to select only the first peak with the largest amplitude on each experimental curve. The rest of the curve was set to zero. Still, in order to take into account the information whether the target was in the air or buried, a little bit different procedure of selecting peaks was implemented. More precisely, the selected peak must be the earliest one with the largest amplitude

$$\text{out of } \begin{cases} \text{all peaks for a buried target,} \\ \text{all downward looking peaks for a target in the air.} \end{cases}$$

Also, since the time moment $\{t = 0\}$ was unknown to us, we set $t := 0$ to be such a point on the time axis, which is one (1) nanosecond to the left from the beginning of the selected peak. Resulting superimposed pre-processed curves are shown on Fig. 5. It is clear now that the condition $t \in (0, \infty)$ in (9) is not a restrictive one, because each curve of Fig. 5 represents a function with a compact support for $t \in (0, \infty)$. It is also clear from comparison of Figures 4-b) and 5 that the pre-processed data are far from the range of the operator $A(\varepsilon_r) := u(0, t)$, which should be inverted to solve CIP1.

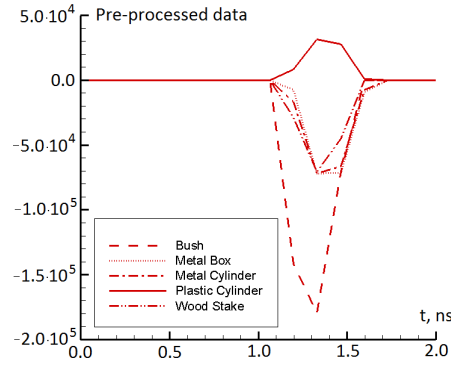


Figure 5: *Pre-processed experimental data from the right panel of Fig. 3.*

2.3.2 Second stage: the choice of the calibration factor

The modulus of the curve of Fig. 4-b) does not exceed 0.2. On the other hand, amplitudes of peaks of experimentally measured curves of Fig. 3 are of the order of 10^4 . This means that the data correspond to $A\delta(x - x_0)$ in (7), where the number $A = \text{const.} > 0$ is unknown. In our experience a similar situation takes place for all experimental data, not necessarily for the current one. It is clear therefore that in order to make the data suitable for the model (6)-(9), they must be multiplied by a certain number, which we call “calibration factor” and denote CF . A proper choice of CF is a non-trivial task. To have unbiased studies, it is *important* that CF must be the same for all targets.

In [24] the same calibration number CF was chosen for all five targets. It is important that because of the blind case, that choice was unbiased. If we would have measured the dielectric constant of at least one target in advance, then we would choose CF in such a way that the number R in (1), which would be obtained via solving the above CIP, would be close to the measured one. However, since dielectric constants were unknown in advance, then another method of choice of CF was used in [24]. Namely, consider the Laplace transform of the function $u(x, t)$,

$$w(x, s) = \mathcal{L}(u(x, t)) := \int_0^{\infty} u(x, t)e^{-st} dt, \quad s \geq \underline{s} = \text{const.} > 0. \quad (10)$$

We call the parameter s pseudo frequency. Denote

$$\begin{aligned} \bar{g}(s) &= \mathcal{L}g, \\ g_0(s) &= \frac{1}{2}\mathcal{L}(H(t - |x_0|)) = \frac{\exp(-s|x_0|)}{2s}, \\ \hat{g}(s) &= \bar{g}(s) - g_0(s). \end{aligned} \quad (11)$$

Let $\widehat{g}_{sim}(s)$ be the Laplace transform of the function depicted on Fig. 4-b). Let $\widehat{g}_{bush}(s)$ be the Laplace transform of the function, which corresponds to bush on Fig. 5. Then we multiply all experimental data by such a calibration number CF that values of functions $\widehat{g}_{sim}(s)$ and $CF \cdot \widehat{g}_{bush}(s)$ would be not far from each other for $s \in [1, 5]$. It was shown in [24] that $CF = 10^{-7}$ was good for this goal. Furthermore, we have discovered that the same value of $CF = 10^{-7}$ provides similar behavior for Laplace transforms of four other curves of Fig. 5. In [24] we have also varied the calibration factor CF by 20% as $CF_1 = 0.8 \cdot 10^{-7}, CF_2 = 1.2 \cdot 10^{-7}$. In all three cases of CF, CF_1 and CF_2 the resulting values of dielectric constants were within tabulated limits [24]. Hence, we have chosen in [24]

$$CF = 10^{-7}. \quad (12)$$

The choice of CF for the GLK is a more delicate issue, and we discuss it in section 5.1.

3 Approximately Globally Convergent Method

In this section we briefly describe the 1-d version of AGCM for CIP1. Details can be found in [24] as well as in section 6.9 of the book [6]. It was proved in [24] that the function $w(x, s)$ in (10) is the solution of the following problem

$$w_{xx} - s^2 \varepsilon_r(x) w = -\delta(x - x_0), x \in \mathbb{R}, \forall s \geq \underline{s}, \quad (13)$$

$$\lim_{|x| \rightarrow \infty} w(x, s) = 0. \quad (14)$$

Denote

$$w(0, s) := \bar{g}(s), \quad s \geq \underline{s}, \quad (15)$$

where the function $\bar{g}(s)$ is defined in (11). It was shown in [24] that

$$w_x(0, s) := \rho(s) = s\bar{g}(s) - \exp(sx_0). \quad (16)$$

3.1 Integral differential equation

Consider the fundamental solution $w_0(x, s)$ of the problem (13), (14) for $\varepsilon_r(x) \equiv 1$. Then

$$w_0(x, s) = \frac{1}{2s} \exp(-s|x - x_0|). \quad (17)$$

Since $w(x, s) > 0$ [24], we can consider $\ln[w(x, s)]$. Denote

$$r(x, s) = \frac{\ln[(w/w_0)(x, s)]}{s^2}. \quad (18)$$

Then (13)-(17) imply that [24]

$$r_{xx} + s^2 r_x^2 - 2sr_x = \varepsilon_r(x) - 1, \quad x > 0, \quad (19)$$

$$r(0, s) = \varphi_0(s), \quad r_x(0, s) = \varphi_1(s), \quad (20)$$

$$\varphi_0(s) = \frac{1}{s^2} [\ln \bar{g}(s) - \ln(2s)] + \frac{x_0}{s}, \quad \varphi_1(s) = \frac{2}{s} - \frac{\exp(sx_0)}{s^2 \bar{g}(s)}, \quad (21)$$

$$r_x(1, s) = 0. \quad (22)$$

Differentiate equation (19) with respect to s . Denote

$$q(x, s) = \partial_s r(x, s), \quad \psi_0(s) = \varphi_0'(s), \quad \psi_1(s) = \varphi_1'(s), \quad (23)$$

$$r(x, s) = - \int_s^{\bar{s}} q(x, \tau) d\tau + V(x, \bar{s}), \quad (24)$$

$$V(x, \bar{s}) = \frac{1}{\bar{s}^2} \{ \ln [w(x, \bar{s})] - \ln [w_0(x, \bar{s})] \} = r(x, \bar{s}). \quad (25)$$

Here $\bar{s} > 0$ is a sufficiently large number which is chosen in numerical experiments. We call $V(x, \bar{s})$ the *tail function*. Actually \bar{s} is one of regularization parameters of this method. We have

$$V(x, \bar{s}) = \frac{p(x)}{\bar{s}} + O\left(\frac{1}{\bar{s}^2}\right), \quad \bar{s} \rightarrow \infty, \quad (26)$$

$$q(x, \bar{s}) = -\frac{p(x)}{\bar{s}^2} + O\left(\frac{1}{\bar{s}^3}\right), \quad \bar{s} \rightarrow \infty. \quad (27)$$

Using (19)-(25), we obtain

$$\begin{aligned} & q_{xx} - 2s^2 q_x \int_s^{\bar{s}} q_x(x, \tau) d\tau + 2s \left[\int_s^{\bar{s}} q_x(x, \tau) d\tau \right]^2 - 2s q_x + 2 \int_s^{\bar{s}} q_x(x, \tau) d\tau \\ & + 2s^2 q_x V_x - 4s V_x \int_s^{\bar{s}} q_x(x, \tau) d\tau + 2s V_x^2 - 2V_x = 0, \quad s \in [\underline{s}, \bar{s}], \end{aligned} \quad (28)$$

$$q(0, s) = \psi_0(s), \quad q_x(0, s) = \psi_1(s), \quad q_x(1, s) = 0, \quad s \in [\underline{s}, \bar{s}]. \quad (29)$$

The main difficulty of this numerical method is in the solution of the problem (28), (29). Equation (28) has two unknown functions q and V . To approximate both of them, we use a scheme, which is based on both inner and outer iterations [23, 24]. First, given an approximation for V , we update q via solution of a boundary value problem on the interval $x \in (0, 1)$. This is our inner iteration. Next, we update the unknown coefficient $\varepsilon_r(x)$ and solve the forward problem (13), (14) for $s := \bar{s}$ on the entire real line \mathbb{R} with this updated coefficient $\varepsilon_r(x)$. Next, we update the tail function $V(x, \bar{s})$ via (25). If both functions q and V are approximated well by functions \tilde{q} and \tilde{V} respectively via this numerical procedure,

then we use backwards calculations (24), (19) to approximate the unknown coefficient $\tilde{\varepsilon}_r(x)$,

$$\tilde{r}(x, s) = - \int_s^{\bar{s}} \tilde{q}(x, \tau) d\tau + \tilde{V}(x, \bar{s}), \quad (30)$$

$$\tilde{\varepsilon}_r(x) = \begin{cases} 1 + \tilde{r}_{xx} + s^2 \tilde{r}_x^2 - 2s \tilde{r}_x, & x \in (0, 1), \\ 1, & x \notin (0, 1). \end{cases} \quad (31)$$

3.2 Numerical procedure

Consider a partition of the interval $[\underline{s}, \bar{s}]$ into N small subintervals with the grid step size $h > 0$ and assume that the function $q(x, s)$ is piecewise constant with respect to s ,

$$\underline{s} = s_N < s_{N-1} < \dots < s_0 = \bar{s}, s_{i-1} - s_i = h; q(x, s) = q_n(x), \text{ for } s \in (s_n, s_{n-1}].$$

For each subinterval $(s_n, s_{n-1}]$ we obtain a differential equation for the function $q_n(x)$. We assign for convenience of notations $q_0 \equiv 0$. For each n we iterate to improve tails. Next, we go to the next n . This way we obtain functions $q_{n,k}, V_{n,k}$. The equation for the pair $(q_{n,k}, V_{n,k})$ is

$$\begin{aligned} q''_{n,k} - \left(A_{1,n} h \sum_{j=0}^{n-1} q'_j - A_{1,n} V'_{n,k} - 2A_{2,n} \right) q'_{n,k} = \\ - A_{2,n} h^2 \left(\sum_{j=0}^{n-1} q'_j \right)^2 + 2h \sum_{j=0}^{n-1} q'_j + 2A_{2,n} V'_{n,k} \left(h \sum_{j=0}^{n-1} q'_j \right) \\ - A_{2,n} (V'_{n,k})^2 + 2A_{2,n} V'_{n,k}, \quad x \in (0, 1), n \in [1, N], k \in [1, m], \end{aligned} \quad (32)$$

where the number m should be chosen in numerical experiments. The boundary conditions are generated by (29),

$$q_{n,k}(0) = \psi_{0,n}, q'_{n,k}(0) = \psi_{1,n}, q'_{n,k}(1) = 0. \quad (33)$$

Boundary conditions (33) are over-determined ones. On the other hand, our attempts to use only two out of three boundary conditions (33) never led to acceptable results [23]. Thus, given the function $V'_{n,k}(x)$, we use all three conditions (33) and find an approximate solution $q_{n,k}(x)$ of the problem (32), (33) via the Quasi-Reversibility Method (QRM), see subsection 3.3. We refer to the book [26] for the originating work about the QRM and to [6, 13, 21, 23, 24] for some follow up publications. QRM is well suited for solving over-determined boundary value problems. Convergence of QRM is proved via Carleman estimates [21].

The choice of the first tail function $V_{1,1}(x)$ is described in subsection 3.3. Let $n \geq 1$. Suppose that for $j = 0, \dots, n-1$ functions $q_j(x), V_j(x)$ are constructed. We now construct functions $q_{n,k}, V_{n,k}$ for $k = 1, \dots, m$. We set $V_{n,1}(x) := V_{n-1}(x)$. If the function $V_{n,k}(x)$ is

given, then we find an approximate solution $q_{n,k}(x)$ of the problem (32), (33). Next, we find the approximation $\varepsilon_r^{(n,k)}$ for the unknown coefficient $\varepsilon_r(x)$ via discrete analogs of (30), (31),

$$r_{n,k}(x) = -hq_{n,k} - h \sum_{j=0}^{n-1} q_j + V_{n,k}, \quad x \in (0, 1),$$

$$\varepsilon_r^{(n,k)}(x) = \begin{cases} 1 + r''_{n,k}(x) + s_n^2 [r'_{n,k}(x)]^2 - 2s_n r'_{n,k}(x), & x \in (0, 1), \\ 1, & x \notin (0, 1). \end{cases}$$

Next, we solve the forward problem (13), (14) with $\varepsilon_r(x) := \varepsilon_r^{(n,k)}(x)$, $s := \bar{s}$ and find the function $w_{n,k+1}(x, \bar{s})$ this way. After this we update the tail via formula (25) in which $w(x, \bar{s}) := w_{n,k+1}(x, \bar{s})$. This way we obtain a new tail $V_{n,k+1}(x)$. Similarly we continue iterating with respect to tails m times. Next, we set

$$q_n(x) := q_{n,m}(x), \quad V_n(x) := V_{n+1,1}(x) := V_{n,m}(x), \quad \varepsilon_r^{(n)}(x) := \varepsilon_r^{(n,m)}(x),$$

replace n with $n + 1$ and repeat this process. By [23] we continue this process until

$$\text{either } \|\varepsilon_r^{(n)} - \varepsilon_r^{(n-1)}\|_{L_2(0,1)} \leq 10^{-5} \text{ or } \|\nabla J_\alpha(q_{n,k})\|_{L_2(0,1)} \geq 10^5, \quad (34)$$

where the functional $J_\alpha(q_{n,k})$ is defined in (35) of subsection 3.3. Here the norm in the space $L_2(0,1)$ is understood in the discrete sense. In the case when the second inequality (34) is satisfied, we stop at the previous iteration taking $\varepsilon_r^{(n,k-1)}(x)$ as our solution. If neither of two conditions (30) is not reached at $n := N$, then we repeat the above sweep over the interval $[\underline{s}, \bar{s}]$ taking the tail $V_N(x)$ as the new tail $V_{1,1}(x)$. Usually at least one of conditions (34) is reached at most on the third or on the fourth sweep, and the process stops then.

3.3 Computing functions $q_{n,k}(x)$, $V_{1,1}(x)$

As it was mentioned in Subsection 3.2, we compute approximations for functions $q_{n,k}(x)$ via QRM. Let $L(q_{n,k})(x)$ be the operator in the left hand side of equation (32) and $P_{n,k}(x)$ its right hand side. Let $\alpha \in (0, 1)$ be the regularization parameter. The QRM minimizes the following Tikhonov regularization functional

$$J_\alpha(q_{n,k}) = \|L_{n,k}(q_{n,k}) - P_{n,k}\|_{L_2(0,1)}^2 + \alpha \|q_{n,k}\|_{H^2(0,1)}^2, \quad (35)$$

subject to boundary conditions (33).

We now describe an important step of choosing the first tail function $V_{1,1}(x)$. Consider the asymptotic behavior (26) and (27) of functions $V(x, \bar{s})$ and $q(x, \bar{s})$ with respect to the truncation pseudo frequency $\bar{s} \rightarrow \infty$. We truncate in (26) and (27) terms $O(1/\bar{s}^2)$ and $O(1/\bar{s}^3)$ respectively. This is somewhat similar with the definition of geometrical optics as a high frequency approximation of the solution of the Helmholtz equation. Hence, for sufficiently large \bar{s}

$$V(x, \bar{s}) \approx \frac{p(x)}{\bar{s}}, \quad q(x, \bar{s}) \approx -\frac{p(x)}{\bar{s}^2}. \quad (36)$$

Hence, setting in equation (28) $s := \bar{s}$ and using (36), we obtain the following *approximate* equation for the function $p(x)$

$$p''(x) = 0, \quad x \in (0, 1). \quad (37)$$

Boundary conditions for the function $p(x)$ can be easily derived from (29) and (36) as

$$p(0) = -\bar{s}^2 \psi(\bar{s}), \quad p'(0) = -\bar{s}^2 \psi_1(\bar{s}), \quad p'(1) = 0. \quad (38)$$

We find an approximate solution $\bar{p}(x)$ of the problem (37), (38) via the QRM. Next, we set for the first tail function

$$V_{1,1}(x) := \frac{\bar{p}(x)}{\bar{s}}. \quad (39)$$

Theorem 1 is a simplified version of Theorem 6.1 of [24], also see Theorem 6.7 of [6] for the 3-d case.

Theorem 1. *Let the function $\varepsilon_r^*(x)$ satisfying conditions (4), (5) be the exact solution of our CIP for the noiseless data $g^*(t)$ in (9). Fix the truncation pseudo frequency $\bar{s} > 1$. Let the first tail function $V_{1,1}(x)$ be defined via (37)-(39). Let $\gamma \in (0, 1)$ be the level of the error in the boundary data, i.e.*

$$|\psi_0(s) - \psi_0^*(s)| \leq \gamma, \quad |\psi_1(s) - \psi_1^*(s)| \leq \gamma, \quad \text{for } s \in [\underline{s}, \bar{s}],$$

where functions $\psi_0(s), \psi_1(s)$ depend on the function $g(t)$ in (9) via (11), (21), (23) and functions $\psi_0^*(s), \psi_1^*(s)$ depend on the noiseless data $g^*(t)$ in the same way. Let $\sqrt{\alpha} = \gamma$ and $\tilde{h} = \max(\gamma, h)$. Let Q be the total number of functions $\varepsilon_r^{(n,k)}$ computed in the above algorithm. Then there exists a constant $D = D(x_0, d_0, d_1, \bar{s}) > 1$ such that if the number \tilde{h} is so small that

$$\tilde{h} < \frac{1}{DQ}, \quad (40)$$

then the following convergence estimate is valid

$$\|\varepsilon_r^{(n,k)} - \varepsilon_r^*\|_{L_2(0,1)} \leq \tilde{h}^\omega, \quad (41)$$

where the number $\omega \in (0, 1)$ is independent on $n, k, \tilde{h}, \varepsilon_r^{(n,k)}, \varepsilon_r^*$.

Theorem 1 guarantees that if the total number Q of computed functions $\varepsilon_r^{(n,k)}$ is fixed and error parameters σ, h are sufficiently small, then iterative solutions $\varepsilon_r^{(n,k)}(x)$ are sufficiently close to the exact solution ε_r^* , and this closeness is defined by the error parameters. Estimate (41) guarantees the stability of AGCM with respect to a small error in the data. Therefore the total number of iterations Q can be considered as one of regularization parameters of our process. Two other regularization parameters are the numbers \bar{s} and α . The combination of inequalities (40) and (41) has a direct analog in the inequality of Lemma 6.2 on page 156 of the book [15] for classical Landweber iterations, which are defined for a substantially different ill-posed problem. Indeed, it is stated on page 157 of the book [15] that the number of iterations can serve as a regularization parameter for an ill-posed problem.

The *main advantage* of Theorem 1 is that even though it does not require any advanced knowledge of a small neighborhood of the exact solution ε_r^* , it still guarantees the most important property of this algorithm: the property of delivering at least one point in this neighborhood. In principle, (41) guarantees that one can take the function $\varepsilon_r^{(1,1)}$ resulting from just the first tail $V_{1,1}(x)$ as an approximate solution. In other words, already on the first iteration we obtain a good approximation. Next, one can proceed either of two ways. First, one can continue iterations as long as the total number Q of iterations satisfies inequality (40). In doing so, one can choose an optimal number of iterations, based on numerical experience, see (34) for our stopping rule. Second, one can choose either of functions $\varepsilon_r^{(n,k)}$ with $nk \leq Q$ as an approximate solution and then refine it using one of locally convergent numerical methods. This is a two-stage numerical procedure, which was developed in [8, 6] and some other publications about AGCM. An effective method of this sort is, e.g. Adaptive Finite Element Method (adaptivity), which minimizes the Tikhonov functional on a sequence of locally refined finite element meshes, see, e.g. [5, 10] and Chapter 4 of the book [6].

In the numerical implementation of AGCM the functional $J_\alpha(q_{n,k})$ in (35) was written via finite differences and was minimized with respect to the values of the function $q_{n,k}$ at grid points. Conjugate gradient method was used for the minimization. Convergence of this method to the unique minimizer of $J_\alpha(q_{n,k})$ follows from the strong convexity of $J_\alpha(q_{n,k})$, which, in turn follows from Lemma 5.2 of [23]. The s -interval was $s \in [\underline{s}, \bar{s}] = [0.5, 12]$. The length of each small subinterval (s_n, s_{n-1}) was $h = 0.5$. We took $\alpha = 0.04$ in (35). For each $n = 1, \dots, N$ we have calculated functions $q_{n,k}$ for $k = 1, \dots, 10 := m$. We refer to [23, 24] for details of the numerical implementation of AGCM for this case.

3.4 Numerical results for AGCM

Test 1. We now test AGCM for computationally simulated data for the case of the function $\varepsilon_r(x)$ displayed on Fig. 4-a). We have introduced the multiplicative random noise in the function $g(t)$ in (9) as

$$g_\xi(t_i) = g(t_i)(1 + \sigma\xi_i), \quad (42)$$

where $t = t_i$ is the discrete value number i of the variable $t \in (0, T)$, which was used in data simulations, $\sigma \in (0, 1)$ is the noise level and ξ_i is the value number i of the random variable $\xi \in (-1, 1)$. Hence, e.g. $\sigma = 0.05$ means 5% of the noise level in the data. Because of Fig. 4-b) as well as because of the rapid decay of the kernel e^{-st} of the Laplace transform (10), we took $T = 4$. Images with 0%, 5% and 10% noise in (42) are displayed on Fig. 6. One can observe that both the location of the abnormality and the maximal value of the coefficient $\varepsilon_r(x)$ are imaged with a good accuracy for all three cases.

Test 2. We now show the image using experimental data for case of “bush”. This case is the most difficult one, since bush is highly heterogeneous. We remind that because our data are severely under-determined ones, the calculated function $R(x)$ in (1) is a sort of a weighted average value of the ratio (1) over the volume of a target. Next, we have applied formulas (2), (3) to find $\varepsilon_r(\text{target})$. We do not reproduce images of other four available cases of real data, since they are published in [24]. Fig. 7 displays this image. Hence, $\bar{R} = 6.4$

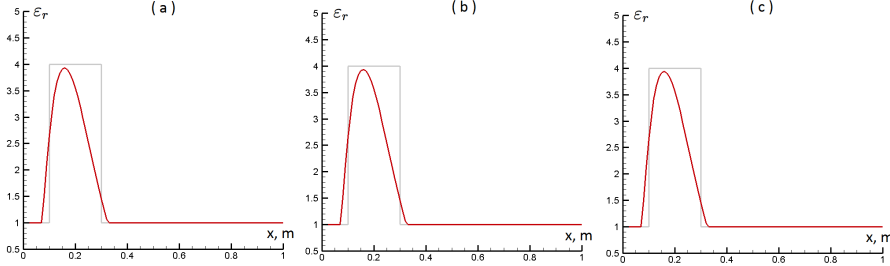


Figure 6: *Images from computationally simulated data for different values of the random noise in the data, see (42). The true target is the same as on Fig. 4-a). a) 0% noise, b) 5% noise, c) 10% noise.*

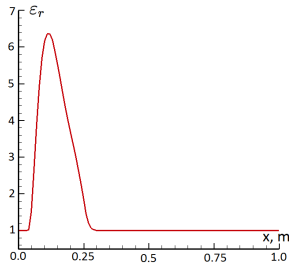


Figure 7: *The blindly computed function $R(x)$ for bush, see the fourth row of Fig. 3. The computed value $\max R(x) = \bar{R} = 6.4 = \varepsilon_r(\text{bush})$ is within tabulated limits of $[3, 20]$ [14]*

in this case. As one can see from Fig. 3, bush was standing in the air. Hence, in this case $\varepsilon_r(\text{bckgr}) = 1$. We conclude therefore that the computed value $\varepsilon_r(\text{bush}) = 6.4$. On the other hand it is clear from [14] that the tabulated value is $\varepsilon_r(\text{bush}) \in [3, 20]$. Therefore, our blindly computed value of the dielectric constant of bush is within tabulated limits.

Table 1 [24] shows computed values for all five cases of experimental data. The background value of the dielectric constant of the dry sand, in which three out of five targets were buried, was between 3 and 5 [32]. It is clear from Fig. 3 which targets were buried and which ones were standing in the air. The dielectric constant for metals is not defined in Physics. Nevertheless, it was established in numerical experiments in [24] that as soon as the value of the dielectric constant of a target $\varepsilon_r \geq 10$, the backscattering electric wave from this target is about the same as the one from a metallic target. Therefore, the so-called *appearing dielectric constant* for metals was introduced in [24], i.e. this is such a dielectric constant, which is between 10 and 30. Thus we assign for this constant

$$\varepsilon_r(\text{metals}) \in [10, 30]. \quad (43)$$

Tabulated values of dielectric constants of the wood stake and plastic cylinder in Table 1 are taken from Tables [32, 33]. As to the bush, see [14]. The tabulated value of ε_r (metal) is taken from (43). Note that published values of dielectric constants are given within certain intervals. Therefore, by (3), values of computed and tabulated ε_r (target) in Table 1 are also given within certain intervals denoted by brackets. This is unlike computed values of \bar{R} .

Table 1: Blindly computed dielectric constants for five targets of Fig. 3 as in (12), by the globally convergent numerical method versus tabulated ones. “1” in the second column means that the target was in the air and “[3, 5]” means that it was buried in the dry sand whose dielectric constant is between 3 and 5 [32].

target	\bar{R}	$\varepsilon_r(bckgr)$	computed ε_r (target)	tabulated ε_r (target)
metal cylinder	4.3	[3, 5]	[12.9, 21.4]	[10, 30], see (43)
metal box	3.8	[3, 5]	[11.4, 19]	[10, 30], see (43)
wood stake	3.8	1	3.8	[2, 6], see [32]
bush (clutter)	6.4	1	6.4	[3, 20], see [14]
plastic cylinder	0.28	[3, 5]	[0.84, 1.4]	1.2, see [33]

Conclusion. Since dielectric constants of targets were not measured in experiments, the only thing we can do is to compare computed values of ε_r (target) with tabulated ones. The *most important* conclusion, which can be drawn from Table 1, is that in five out of five blind cases computed values of dielectric constants of targets were well within tabulated limits. We remind that the variation of the calibration factor $CF = 10^{-7}$ in (12) by 20% has also resulted in values being well within tabulated limits.

4 The Gelfand-Levitan-Krein Integral Equation (GLK)

4.1 Forward and inverse problems

The forward problem in this case is

$$\varepsilon_r(x)u_{tt} = u_{xx}, \quad x > 0, \quad t > 0, \quad (44)$$

$$u(x, 0) = u_t(x, 0) = 0, \quad (45)$$

$$u_x|_{x=0} = \delta(t). \quad (46)$$

Coefficient Inverse Problem 2 (CIP2). Determine the function $\varepsilon_r(x)$ in (44), assuming that the following function $f(t)$ is known

$$u(0, t) = f(t), \quad t \geq 0. \quad (47)$$

Without loss of generality, we assume that

$$\varepsilon_r(0) = 1. \quad (48)$$

Change the spatial variable as

$$x \Leftrightarrow z = \tau(x) = \int_0^x \sqrt{\varepsilon_r(\tau)} d\tau. \quad (49)$$

Hence, taking into account (48), we obtain that (47) holds at $z = 0$ and (44)-(46) imply that

$$u_{tt} = u_{zz} - \frac{\sigma'(z)}{\sigma(z)} u_z, \quad z > 0, \quad t > 0, \quad (50)$$

$$u(z, 0) = u_z(z, 0) = 0, \quad (51)$$

$$u_z|_{z=0} = \delta(t), \quad (52)$$

$$\sigma(z) = \frac{1}{\sqrt{\varepsilon_r(\tau^{-1}(z))}}. \quad (53)$$

Consider even extensions of functions $\sigma(z)$ and $u(z, t)$ in $\{z < 0\}$. To do this, we set without changing notations $\sigma(z) = \sigma(-z)$, $u(z, t) = u(-z, t)$ for $z < 0$. It follows from [12] that we obtain then the following Cauchy problem

$$u_{tt} = u_{zz} - \frac{\sigma'(z)}{\sigma(z)} u_z, \quad z \in \mathbb{R}, \quad t > 0,$$

$$u(z, 0) = 0, \quad u_t(z, 0) = -2\delta(z).$$

Hence,

$$u(z, t) = -\sqrt{\sigma(z)} \cdot H(t - |z|) + \tilde{u}(z, t), \quad (54)$$

where the function $\tilde{u}(z, t)$ is continuous for $(z, t) \in \mathbb{R} \times (0, T)$, $\forall T > 0$ and $\tilde{u}(z, t) = 0$ for $t \leq |z|$. Hence, (53) and (54) imply that $f(0^+) = u(0^+, 0^+) = -\sqrt{\sigma(0)}$. Combining this with (48), we obtain

$$f(0^+) = -1. \quad (55)$$

Let

$$\hat{f}(t) = \begin{cases} f(t), & t > 0 \\ -f(-t) & t < 0 \end{cases}.$$

Hence, the function $\hat{f}(t)$ is odd and its first derivative $\hat{f}'(t)$ is even. Choose a number $T > 0$. Taking into account (55) and using results of [12, 18], we obtain that the GLK equation has the form

$$w(z, t) - \frac{1}{2} \int_{-z}^z \hat{f}'(t - \tau) w(z, \tau) d\tau = \frac{1}{2}, \quad t \in [-z, z], \quad \forall z \in [0, T/2]. \quad (56)$$

This is not a Volterra equation, because $z \in [0, T/2]$ is a parameter here. Hence, equation (56) should be solved for all values of the parameter $z \in [0, T/2]$. The solution of this equation is connected with the function $\sigma(z)$ via [12, 18]

$$\lim_{t \rightarrow z^-} w(z, t) := w(z, z^-) = \frac{1}{2\sqrt{\sigma(z)}}, \quad z \in [0, T/2]. \quad (57)$$

Hence, by (53) and (57)

$$\varepsilon_r(\tau^{-1}(z)) = \frac{1}{16w^4(z, z^-)}. \quad (58)$$

Therefore, in order to solve CIP2, one needs first to solve equation (56) for all $z \in [0, T/2]$. Next, one needs to reconstruct the function $\varepsilon_r(\tau^{-1}(z))$ via (58). Finally, one needs to change variables backwards transforming z into x via inverting (49).

Theorem 2 [12, 31]. *Let the function $f(t)$ be given for $t \in [0, T]$ for a certain value of $T > 0$. Suppose that there exists unique function $\varepsilon_r(x)$ of CIP2 satisfying conditions (4), (5), in which \mathbb{R} is replaced with $\{x \geq 0\}$. Also, assume that condition (48) holds. Let $\tau(z)$ be the function defined in (49). Then solution of the GLK integral equation (56) exists for each $z \in [0, T/2]$ and is unique. And vice versa: if the function $f(t)$ is known for all $t \in [0, T]$ and the integral equation (56) has unique solution for each $z \in [0, T/2]$, then CIP2 has the unique solution $\varepsilon_r(x)$ for $x \in [0, \tau^{-1}(T/2)]$ satisfying above conditions.*

4.2 Performance of GLK for computationally simulated data

In this subsection we present results of our computations for GLK for computationally simulated data. For our testing we choose the coefficient $\varepsilon_r(x)$ whose graph is depicted on Fig. 4-a). This is the same function as the one for AGCM. We use the FDM to solve the forward problem (44)-(46). The solution of this problem generates the data $f(t) := u(0, t)$, $t \in [0, \tilde{T}]$, where $\tilde{T} > 0$ is a certain number. To verify the stability of our computations with respect to the noise in the data, we introduce the random noise in the data as in (42), where $g(t)$ is replaced with $f(t)$ and T is replaced with \tilde{T} .

Next, we use the change of variables $x \Leftrightarrow z$ in (49) and define the time interval $t \in (0, T)$, $T = T(\tilde{T})$. Indeed, since in (56) $z \in [0, T/2]$ and $t \in [-z, z]$, then the value of $z_{\max} = T/2$ should be such that $\tau^{-1}(z_{\max}) := x_{\max} \geq 1$. Note that all what we need is a lower estimate of z_{\max} rather than its exact value. Hence, to get such an estimate, it is sufficient to know a lower estimate for the unknown coefficient $\varepsilon_r(x)$ rather than the function $\varepsilon_r(x)$ itself. Let

$$\{z_n\}_{n=0}^{M_z} \subset [0, T/2], 0 = z_0 < z_1 < \dots < z_{M_z} = T/2$$

be a partition of the interval $z \in [0, T/2]$ into M_z small subintervals with the grid step size $h_z = z_n - z_{n-1}$. For each z_n we approximate the integral (56) via the trapezoidal rule. For the variable $t \in [-z_n, z_n]$ we use discrete values $\{t_k = \pm z_k\}_{k=-n}^{k=n}$. Next, we solve the resulting linear algebraic system for each z_n and find the discrete function $w(z_n, t_k)$, $\forall k \in [-n, n]$, $\forall n \in [0, M_z]$. Next, we find the discrete function $\varepsilon_r(\tau^{-1}(z_n))$ via (58). Finally, we

numerically invert (49) and find the discrete function $\tilde{\varepsilon}_r(x_n)$ for a certain partition $\{x_n\}_{n=0}^{M_z}$ of the interval $[0, x_{\max}] \supseteq [0, 1]$. This discrete function $\tilde{\varepsilon}_r(x_n)$ is an approximate solution of CIP2.

Since the differentiation of noisy data is an unstable procedure and $\hat{f}'(t - \lambda)$ is the kernel of the integral equation (56), we calculate the derivative $\hat{f}'(t)$ in a special way. For each point $t_k := z_k, k = 1, \dots, M_z - 1$ we approximate the derivative $\hat{f}'(t_k)$ as

$$\hat{f}'(t_k) \approx \frac{\hat{f}(t_{k+1}) - \hat{f}(t_{k-1})}{2h_z}. \quad (59)$$

Next, we extend this approximation as the discrete even function for $t_k = -z_k, k = 1, \dots, M - 1$. Even though (59) seems to be a non-regularizing procedure, it works quite well for our goal, since in the discrete integration in (56) the right hand side of (59) is actually multiplied by $h_z/2$.

We test GLK for 0%, 5% and 10% noise in the data $f(t)$. Let M_x and h_x be the number of grid points and the mesh size respectively for the variable $x \in (0, 1)$. We took $M_x = 250$, which led to $h_x = 0.004$. After the change of variables (49) we got $z \in [0, 1.168]$, $M_z = 349$, $h_z = 3.34 \cdot 10^{-3}$. Results of computations are displayed on Fig. 8-a)-f). Note that Figures 8-a), c), e) depict the function

$$\bar{f}(t) = -\frac{1}{4}(f(t) + 1). \quad (60)$$

Comparison of Figures 8-b), d), f) with Figures 6-a), b), c) shows that GLK better images the shape of the target than AGCM. The inclusion/background contrast $\max \varepsilon_r(x)$ is computed accurately by both GLK and AGCM. On the other hand, the contrast computed by AGCM does not change when the level of noise changes, while it does change for GLK.

5 Comparison of AGCM and GLK on Real Data

As it was pointed out in subsection 2.3.2, to work with experimental data, it is necessary to figure out the calibration factor. This factor was established for AGCM as $CF = 10^{-7}$, see (12). Since dielectric constants of targets were not measured in experiments, while $CF = 10^{-7}$ still led to acceptable values of those constants, then we believe that the best is to use computed values of \bar{R} in Table 1 to figure out the calibration factor for GLK. Thus, we proceed as described in Subsection 5.1.

5.1 The choice of the calibration factor for GLK

The procedure of this choice consists of the following three steps:

Step 1. Select any target X listed in Table 1. We call X ‘‘calibration target’’. Let $F_X(t)$ be the data for the target X , which are pre-processed as in subsection 2.3.1, see Fig. 5.

Step 2. Let $R_{GLK}(X)$ and $R_{AGCM}(X)$ be the function $R(x)$ in (1) computed by GLK and AGCM respectively for the target X . Let $\bar{R}_{GLK}(X)$ and $\bar{R}_{AGCM}(X)$ be corresponding values

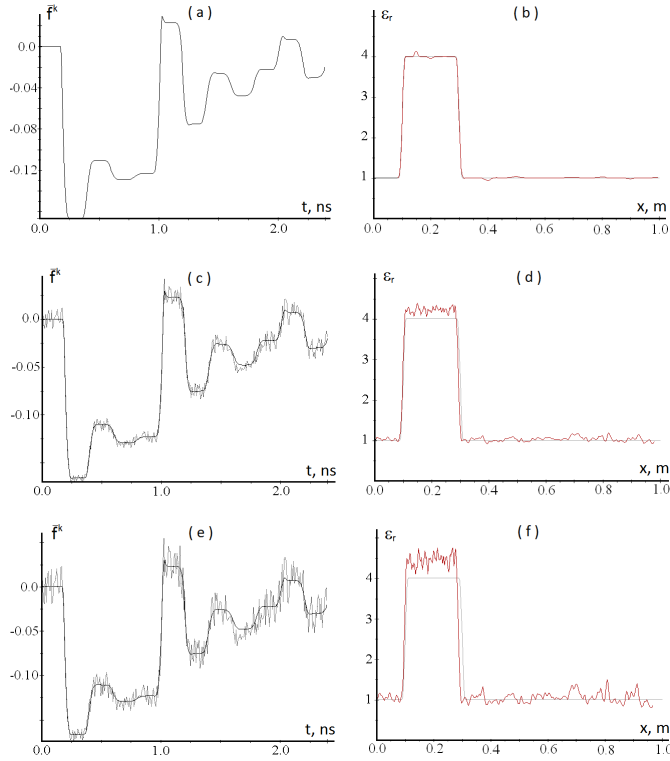


Figure 8: *Performance of GLK for the computationally simulated data for the target of Fig. 4-a). a), c) and e) the computed function $\bar{f}(t)$ in (60) for 0%, 5% and 10% noise respectively. b), d) and f) computed function $\varepsilon_r(x)$ for cases a), c) and e) respectively.*

of the number \bar{R} in (2). Hence, $\bar{R}_{AGCM}(X)$ is the number \bar{R} for the target X in Table 1. Let $CF(X)$ be the calibration factor for GLK. Thus, GLK should be computed for the data $CF(X) \cdot F_X(t)$. Choose such a calibration factor $CF(X)$ that $\bar{R}_{GLK}(X) = \bar{R}_{AGCM}(X)$. Thus, $\bar{R}_{GLK}(X)$ is computed via GLK for the data $CF(X) \cdot F_X(t)$ and $\bar{R}_{AGCM}(X)$ is computed via AGCM for the data $10^{-7}F_X(t)$, see (12).

Step 3. Let $Y \neq X$ be any other target listed in Table 1. When applying GLK to the data $F_Y(t)$, use the same calibration factor $CF(X)$.

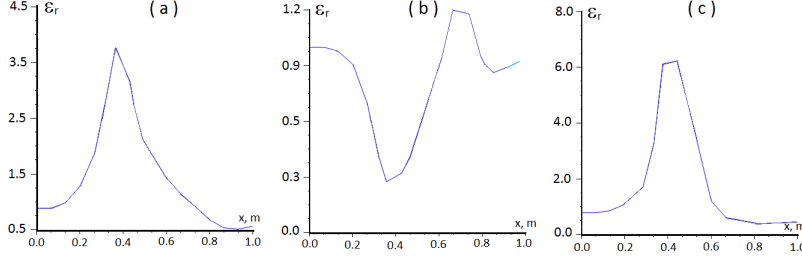


Figure 9: a) The function $R_{GLK}(x)$ for the wood stake when it was the calibration target. Here $CF(\text{wood stake}) = 10^{-5}$, $\bar{R}_{GLK} = 3.8$; b) the function $R_{GLK}(\text{plastic cylinder})$ for the case when the plastic cylinder was the calibration target. Here $CF(\text{plastic cylinder}) = 1.8 \cdot 10^{-5}$, $\bar{R}_{GLK}(\text{plastic cylinder}) = 0.28$; c) the function $R_{GLK}(\text{bush})$ for the case when bush was the calibration target. Here $CF(\text{bush}) = 0.6 \cdot 10^{-5}$, $\bar{R}_{GLK}(\text{bush}) = 6.4$.

5.2 Results

When applying GLK to the pre-processed data, we have chosen T to be the moment of time which is 1.33 nanoseconds to the right from the end of the selected peak.

Case 1. Wood stake is the calibration target. Using Step 2 of Subsection 5.1, we have obtained $CF(\text{wood stake}) = 10^{-5}$. Figure 9-a displays the function $R_{GLK}(\text{wood stake})$.

Table 2: Case 1. Computed numbers \bar{R}_{GLK} for four other targets in comparison with the values of \bar{R} taken from Table 1. Here wood stake was the calibration target. Bold faced is an unrealistic value of \bar{R}_{GLK} .

Target	\bar{R}_{GLK}	\bar{R} from Table 1
metal cylinder	3.25	4.3
metal box	3.97	3.8
plastic cylinder	0.6	0.28
bush	42.5	6.4

We observe from Table 2 that the value $\bar{R}_{GLK}(\text{bush}) = 42.5$ is significantly overestimated compared with the published interval $\bar{R} \in [3, 20]$ in [14].

Case 2. Plastic cylinder is the calibration target. We have obtained $CF(\text{plastic cylinder}) = 1.8 \cdot 10^{-5}$. Figure 9-b displays the function $R_{GLK}(\text{plastic cylinder})$ with this calibration factor.

Table 3: Case 2. Computed numbers \overline{R}_{GLK} for four other targets in comparison with values of \overline{R} taken from Table 1. Here plastic cylinder was the calibration target. Bold faced are those values of \overline{R}_{GLK} which result in unrealistic values of dielectric constants.

Target	\overline{R}_{GLK}	\overline{R} from Table 1
metal cylinder	9.8	4.3
metal box	13.9	3.8
wood stake	17	3.8
bush	>>100	6.4

We observe from Table 3 that the values of \overline{R}_{GLK} for the wood stake and bush are significantly overestimated, compared with the published intervals $[2, 6]$ of [32] and $[3, 20]$ of [14] respectively. Actually we had a blow in the image of bush via GLK in this case.

Case 3. Bush is the calibration target. We have obtained $CF(\text{bush}) = 0.6 \cdot 10^{-5}$. Figure 9-c) displays the function $R_{GLK}(\text{bush})$ with this calibration factor.

Table 4: Case 3. Computed numbers \overline{R}_{GLK} for four other targets in comparison with values of \overline{R} taken from Table 1. Here bush was the calibration target. Bold faced are those values of \overline{R}_{GLK} which lead to unrealistic values of dielectric constants.

Target	\overline{R}_{GLK}	\overline{R} from Table 1
metal cylinder	2.0	4.3
metal box	1.16	3.8
wood stake	2.2	3.8
plastic cylinder	0.74	0.28

It follows from Table 4 that the value of \overline{R}_{GLK} for metal box is significantly underestimated. Indeed, since in the dry sand, which was the background here, $\varepsilon_r \in [3, 5]$ [32], then, using (2), we obtain $\varepsilon_r(\text{metal box}) \in [3.48, 5.8]$. On the other hand, by (43) we should have $\varepsilon_r(\text{metal box}) \in [10, 30]$. Thus, we have the underestimation of $\varepsilon_r(\text{metal box})$ by the factor of 1.72. In addition, the value of \overline{R}_{GLK} for plastic cylinder is overestimated in Table 4. Indeed, since $\varepsilon_r(\text{background}) \in [3, 5]$, then it follows from this table that $\varepsilon_r(\text{plastic cylinder}) \in [2.22, 3.7]$. On the other hand, Table [33] tells us that we should have $\varepsilon_r(\text{plastic cylinder}) \approx 1.2$. Hence, we have overestimation of $\varepsilon_r(\text{plastic cylinder})$ by the factor of 1.85.

Our calculations for the case when metal box was chosen as calibration target led to the same results as those in Table 2. This is because $\overline{R}_{AGCM}(\text{wood stake}) = \overline{R}_{AGCM}(\text{metal box}) = 3.8$. Also, $\overline{R}_{AGCM}(\text{metal cylinder}) = 4.3 \approx \overline{R}_{AGCM}(\text{metal box})$. Hence, the calculation for the case when the metal cylinder was chosen as calibration target again led to results similar with those of Table 2.

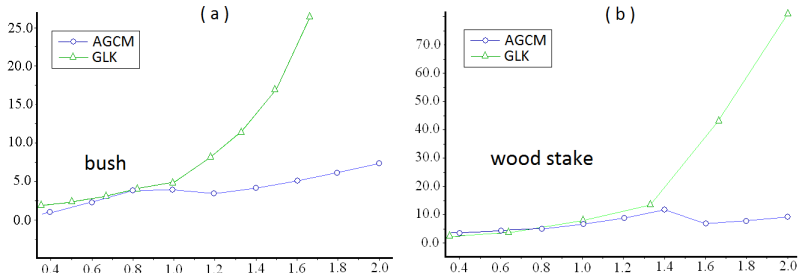


Figure 10: Dependencies of \bar{R}_{AGCM} and \bar{R}_{GLK} from the calibration factor for bush and wood stake are displayed. In both a), b) “1” for AGCM corresponds to $CF = 10^{-7}$, see (12). a) “1” corresponds $CF(\text{bush}) = 0.6 \cdot 10^{-5}$ (Case 3). b) “1” corresponds $CF(\text{wood stake}) = 10^{-5}$.

To see how the changes in the calibration factor affect the reconstructed values of \bar{R}_{AGCM} and \bar{R}_{GLK} , we present Figures 10. The visual analysis of these curves shows that the increase of the calibration factor affects \bar{R}_{AGCM} linearly, and it affects \bar{R}_{GLK} exponentially. This explains results of above Cases 1-3.

6 Discussion

Theorem 2 guarantees existence and uniqueness of the solution of the GLK equation only when the data $f(t)$ belongs to the range of the operator of the forward problem, i.e. for the case of errorless data. However, in the realistic case of an error in the data, stability with respect to this error is not guaranteed by Theorem 2. Hence, the question about regularizing properties of GLK remains open. On the other hand, estimate (41) of Theorem 1 ensures stability of AGCM with respect to a small error in the data, and the same is true for the 3-d version of this method [6, 9, 25].

We have used both computationally simulated and experimental data to compare numerical performances of two methods: GLK and AGCM. In the case of computationally simulated data, the above difference between Theorems 1 and 2 is slightly reflected in the different behavior of computed inclusion/background contrasts in the presence of noise: these contrasts were not changing with noise in the data for AGCM and were slightly changing for GLK. On the other hand, in the case of the above synthetic data, GLK provides better images of shapes of targets, compared with AGCM.

As it was pointed out in subsection 2.3.2, to have unbiased studies of these experimental data, it is important that the calibration factor should be chosen the same for all five targets of Table 1. However, it was shown in subsection 5.2 that it is impossible to choose such a calibration factor for GLK, which would provide satisfactory values of inclusion/background contrasts for all five targets. On the other hand, AGCM has worked successfully with the

uniform calibration factor $CF = 10^{-7}$ for all five targets in the case of blind data. We point out that these conclusions are relevant only for the specific case of the above set of experimental data and for the above specific data pre-preprocessing procedure. On the other hand, we do not possess other sets of 1-d experimental data at the moment, and we are also unaware about other appropriate data pre-processing procedures.

To explain Fig. 10, we present the GLK equation (56) as

$$w(z, t) - \frac{CF(X)}{2} \int_{-z}^z \hat{f}'(t - \tau) w(z, \tau) d\tau = \frac{1}{2}, \quad t \in [-z, z], \quad \forall z \in [0, T/2]. \quad (61)$$

In (61) $f(t)$ is the pre-processed data as in subsection 2.3.1 and $\hat{f}(t)$ is the odd extension of $f(t)$. Denote $\beta := z \cdot CF(X) \sup_{|t| < T/2} |\hat{f}'(t)|$. If $\beta \in (0, 1)$, then one can solve integral equation (61) via the resolvent series, see, e.g. the book [35]. It is clear from this series that the solution $w(z, t)$ changes almost with an exponential speed when the calibration factor $CF(X)$ changes. This explains, at least partially, the exponential behavior of GLK curves of Fig. 10. This is because the data for the inverse problem are introduced in the operator.

On the other hand, almost linear behavior of AGCM curves on Fig. 10 can be explained by the fact that AGCM uses the logarithm of the solution w of the problem (13), (14), see (18).

Acknowledgments

This research was supported by US Army Research Laboratory and US Army Research Office grant W911NF-11-1-0399, Integration project number 14 of Siberian Branch of Russian Academy of Science (SB RAS), Collaboration project number 12-2013 between SB RAS and NAS of Ukraine, and grant 12-01-00773 of Russian Foundation of Basic Research.

References

- [1] A.S. Alekseev and V.I. Dobrinskii, Some questions of the practical usage of dynamic inverse problems of seismics, in *Mathematical Problems of Geophysics*, published by Computing Center of the Siberian Branch of the USSR Academy of Science, Novosibirsk (in Russian) **6**, Part 2 (1975), 7-53.
- [2] A.S. Alekseev and V.S. Belonosov, Scattering of plane waves in inhomogeneous half-space. *Applied Mathematical Letters* **8** (1995), 13-19.
- [3] A.S. Alekseev and V.S. Belonosov, Direct and inverse problems of wave propagation through a one-dimensional inhomogeneous medium, *European Journal of Applied Mathematics*, **10** (1999), 79-96.
- [4] A.B. Bakushinskii and M.Yu. Kokurin, *Iterative Methods for Approximate Solution of Inverse Problems*, Springer, New York, 2004.

- [5] L. Beilina, Adaptive finite element/difference method for inverse elastic scattering waves, *Applied and Computational Mathematics* **1** (2002), 158-174.
- [6] L. Beilina and M.V. Klibanov, *Approximate Global Convergence and Adaptivity for Coefficient Inverse Problems*, Springer, New York, 2012.
- [7] L. Beilina and M. V. Klibanov. A globally convergent numerical method for a coefficient inverse problem, *SIAM J. Sci. Comp.* **31** (2008), 478-509.
- [8] L. Beilina and M.V.Klibanov, Reconstruction of dielectrics from experimental data via a hybrid globally convergent/adaptive inverse algorithm, *Inverse Problems* **26** (2010), 125009.
- [9] L. Beilina and M.V. Klibanov, A new approximate mathematical model for global convergence for a coefficient inverse problem with backscattering data, *J. Inverse and Ill-Posed Problems* **20** (2012), 513-565.
- [10] L. Beilina and M.V. Klibanov, Relaxation property for the adaptivity for ill-posed problems, posted online of *Applicable Analysis* at <http://dx.doi.org/10.1080/00036811.2013.768339>.
- [11] L. Beilina, Energy estimates and numerical verification of the stabilized domain decomposition finite element/finite difference approach for the Maxwell's system in time domain, *Central European Journal of Mathematics*, 11 (2013), 702-733.
- [12] A.S. Blagoveshenskii, On a local method of solving a non-stationary inverse problem for inhomogeneous string, *Proceedings of Mathematical Steklov Institute* **115** (1971), 28-38 (in Russian).
- [13] L. Bourgeois, Convergence rates for the quasi-reversibility method to solve the Cauchy problem for Laplace's equation, *Inverse Problems*, 22, 413-430, 2006.
- [14] H.T. Chuah, K.Y. Lee and T.W. Lau, Dielectric constants of rubber and oil palm leaf samples at X-band, *IEEE Trans. on Geoscience and Remote Sensing* **33** (1995), 221-223
- [15] H.W. Engl, M. Hanke and A. Neubauer, *Regularization of Inverse Problems*, Kluwer Academic Publishers, Boston, 2000.
- [16] I.M. Gel'fand and B.M. Levitan, On the determination of a differential equation from its spectral function, *American Mathematical Society Translations* **1** (1955), 253-304.
- [17] G.M. Henkin and N.N. Novikova, The reconstruction of the attracting potential in the Sturm-Liouville equation through characteristics of negative discrete spectrum, *Studies in Applied Mathematics*, 97, 17-52, 1996.
- [18] S.I. Kabanikhin, A.D. Satybaev and M.A. Shishlenin, *Direct Methods of Solving Multi-dimensional Inverse Hyperbolic Problems*, VSP, Utrecht, 2004.

- [19] S. I. Kabanikhin and M.A. Shishlenin, Numerical algorithm for two-dimensional inverse acoustic problem based on Gel'fand-Levitan-Krein equation, *J. Inverse and Ill-Posed Problems* **18** (2011), 979-995.
- [20] M. V. Klibanov, M. A. Fiddy, L. Beilina, N. Pantong and J. Schenk, Picosecond scale experimental verification of a globally convergent numerical method for a coefficient inverse problem, *Inverse Problems* **26** (2010), 045003.
- [21] M. V. Klibanov, Carleman estimates for global uniqueness, stability and numerical methods for coefficient inverse problems, *J. Inverse and Ill-Posed Problems* **21** (2013), to appear.
- [22] M.G. Krein, A method of efficient solution of an inverse boundary value problem, *Dokl. Acad. Nauk USSR* **94** (1954), 987-990 (in Russian).
- [23] A.V. Kuzhuget and M.V. Klibanov, Global convergence for a 1-D inverse problem with application to imaging of land mines, *Applicable Analysis* **89** (2010), 125-157.
- [24] A.V. Kuzhuget, L. Beilina, M.V. Klibanov, A. Sullivan, L. Nguyen and M.A. Fiddy, Blind experimental data collected in the field and an approximately globally convergent inverse algorithm, *Inverse Problems* **28** (2012), 095007.
- [25] A.V. Kuzhuget, L. Beilina and M.V. Klibanov, Approximate global convergence and quasi-reversibility for a coefficient inverse problem with backscattering data, *J. of Mathematical Sciences*, **181** (2012), 19-49.
- [26] R. Lattes and J.-L. Lions, *The Method of Quasireversibility: Applications to Partial Differential Equations*, Elsevier, New York, 1969.
- [27] B.M. Levitan, *Inverse Sturm-Liouville Problems*, VSP, Utrecht, 1987.
- [28] V.M. Markushevich, N.N. Novikova, T.A. Povzner, I.V. Savin and V.E. Fedorov, The method of acoustic profile reconstruction from normal monochromatic waves, *Computational Seismology*, **19** (1986), 135-145.
- [29] R.G. Novikov and M. Santacesaria, Monochromatic reconstruction algorithms for two-dimensional multi-channel inverse problems, *International Mathematics Research Notices*, accepted for publication, available online at <http://imrn.oxfordjournals.org/cgi/content/abstract/rns025?>
- [30] N. Nguyen, D. Wong, M. Ressler, F. Koenig, B. Stanton, G. Smith, J. Sichina and K. Kappra, Obstacle avoidance and concealed target detection using the Army Research Lab ultra-wideband synchronous impulse Reconstruction (UWB SIRE) forward imaging radar, *Proc. SPIE* **6553** (2007), 65530H (1)-65530H (8)
- [31] V.G. Romanov, *Inverse Problems of Mathematical Physics*, VNU, Utrecht, 1986.

- [32] Tables of dielectric constants at <http://www.asiinstr.com/technical/Dielectric0Constants.htm>.
- [33] Tables of dielectric constants at http://www.krohne.com/Dielectric_Constants.6840.0.html.
- [34] A.N. Tikhonov, A.V. Goncharsky, V.V. Stepanov and A.G. Yagola, *Numerical Methods for the Solution of Ill-Posed Problems*, Kluwer, London, 1995.
- [35] V.S. Vladimirov, *Equations of Mathematical Physics*, New York, M. Dekker, 1971.